UDC 551.511.33:551.521.3:551.508.25:551.515

RADIATION MODELS OF MIDLATITUDE SYNOPTIC FEATURES

STEPHEN K. COX

Department of Meteorology, University of Wisconsin, Madison, Wis.

ABSTRACT

Balloon-borne radiation sonde measurements during 1964 and 1965 are used to form composite, three-dimensional radiative cooling models for the following midlatitude synoptic features: stationary front; nascent cyclone; warm sector cyclone; occluded cyclone; and anticyclone. Composite water vapor distributions for the same synoptic features are used to model the pattern of atmospheric warming by solar radiation.

Thickness tendency analyses of the 1000–500-mb layer for four synoptic features show that radiative cooling and warming may account for 10–30 percent of the observed maximum thickness tendency. The radiative thickness change components are of the same order of magnitude as the latent and the sensible heating terms.

The nascent cyclone case shows a radiatively induced vorticity tendency of 6×10^{-10} sec^{-2}. This compares with a total expected vorticity tendency between 10^{-9} and 10^{-10} sec^{-2}. The nascent cyclone, warm sector cyclone, and anticyclone cases show positive cyclonic development from radiative effects, while the occluded cyclone case shows negative cyclonic development.

1. INTRODUCTION

Many investigators have conjectured that radiative effects may be neglected for periods as long as days without materially affecting synoptic scale development; however, this has not been shown to be fact. Sutcliffe (1947) acknowledges this attitude and expresses reservations about the neglect of radiative effects, even for relatively short time scales. Suomi and Chen (1963) show that infrared cooling significantly affects the generation of available potential energy (APE) on a synoptic scale. Dutton and Johnson (1967) suggest that the generation of APE caused by radiative processes in a synoptic system varies with time and may become significant at some point in its life cycle. Anthes (1968) shows that infrared cooling may account for 17 percent of the generation of APE in a hurricane.

One may attempt to answer the question of the importance of radiation effects on synoptic scale phenomena by computing the radiative energy transfer through the atmosphere. However, this technique is hampered by an insufficient understanding of radiative transfer in a cloudy atmosphere. Even if radiative transfer through clouds were clearly understood, one faces the monumental task of defining cloud characteristics and structure before proceeding with model calculations.

This paper describes infrared cooling radiation models of classical synoptic features constructed from direct measurements of infrared radiation. Short-wave radiation models are produced by applying the techniques of Hanson et al. (1967) to composite maps of the water vapor distribution.

In general, the symbols follow standard meteorological usage; however, the following list of symbols and abbreviations may be helpful to the reader.

A	Empirical constant used to vertically partition solar absorption
APE	Available potential energy
c_p	Specific heat of dry air at constant pressure
dH/dt	Rate of diabatic heating
E	Solar energy absorbed by the atmosphere
IR	Infrared radiation
p_0	Surface of pressure
q_a	Fractional absorption of solar energy
Q_0	Vorticity at the surface
S	Solar constant
SW	Short-wave radiation
$\mathbf{V}_0$	Velocity at surface
U	Optical depth of water vapor
U^*	Optical path of water vapor ($U^*=U\times\sec(\theta)$)
Γ_d	$=\frac{1}{\rho g}\gamma_d$
Γ	$=\frac{1}{\rho g}\gamma$
ϕ	Latitude
ϕ_0	Center latitude of gridded models, 40° N.
λ	Longitude
λ_0	Center longitude of gridded models, 95° W.
θ	Solar zenith angle

2. MODEL CONFIGURATIONS

In order to make a composite model of the radiation soundings, it is necessary to define a configuration for each model and then normalize all similar synoptic features to that configuration. All radiation sonde ascents are grouped according to their proximity to a synoptic feature as determined from surface maps. Some soundings are included in two or more categories when they are located between closely spaced synoptic features.

The features examined the number of soundings in each category and the model configurations are given below:

a) *Stationary front*—number of soundings: 17. The stationary front model was assumed to be oriented east to west along 40° N. latitude. All soundings in the vicinity of a stationary front were plotted as a north-south cross section, their separation from the east-west model front being the perpendicular distance to the front in the observed case.

b) *Nascent cyclone*—number of soundings: 47. The nascent cyclone model was chosen to be on an east-west-oriented frontal system with the center of the depression acting as the origin of a polar coordinate system. For the model case, 180° was assigned to the open part of the wave south of the depression and 180° to the area north of the front. All soundings in the proximity of nascent cyclones were normalized to this model configuration. An angle and radial distance were sufficient to define the position of a sounding in the composite model.

c) *Warm sector cyclone*—number of soundings: 86. The warm sector cyclone model was defined so that the cold front extended straight south and the warm front east with the center of the Low at ϕ_0, λ_0. All observed cases were normalized to agree with the configuration with a 90° warm sector and 270° on the back side and north of the Low. Here again the center of the Low was treated as the origin of a polar coordinate system, and an angle and radial distance were sufficient to define the position in the composite model.

d) *Occluded cyclone*—number of soundings: 54. The occluded cyclone model was constructed in nearly the same way as the warm sector model, the only difference being that the center of the polar coordinate system was taken as the point of occlusion rather than at the low-pressure center. As a result, the occluded front is in the northwest sector of a model.

e) *Anticyclone*—number of soundings: 112. The anticyclone model was constructed with the center of the High as the center of a polar coordinate system.

The infrared radiation data and mixing ratio data for all soundings used in this study were placed in the appropriate synoptic categories, and normalized angles and radial distances were computed to form the composite radiation models.

3. LONG-WAVE RADIATION ANALYSIS

During 1964 and 1965, approximately 180 International Quiet Sun Year (IQSY) radiation sonde ascents were made from U.S. Weather Bureau (USWB) upper air stations at Green Bay, Wis., and Sterling, Va. In addition, in December 1965 a series of radiation sonde ascents was made from a network of midwestern USWB upper air stations in a study organized by the University of Wisconsin. All measurements were made with a Suomi-Kuhn net radiation sonde (Tanner et al., 1960), and temperature and moisture profiles were measured simultaneously. These soundings are used in this study and represent all four seasons and include the fall and winter seasons from 2 yr.

The radiation soundings referred to above were grouped according to synoptic features and gridded as described in section 2.

4. SHORT-WAVE RADIATION ANALYSIS TECHNIQUE

Hanson et al. (1967) have given equation (1) as an empirical relationship between q_a, the fractional absorption of solar radiation in an atmospheric column, and U^*, the optical path length of water vapor.

$$q_a = 0.096 + 0.045\ U^{*1/2} \log U^*. \tag{1}$$

This expression was derived from satellite and surface radiation measurements over the United States. Equation (1) inherently includes the effects of clouds, since the data from which it was derived included both clear and cloudy cases. The short-wave data in figure 1 illustrating the vertical partitioning of radiative divergence in a cloudy atmosphere are taken from Korb and Möller (1962). These values of short-wave absorption are based upon a theoretical result for a stratified cloud, 1000 m thick for a solar zenith angle of zero degrees. A ground albedo of zero and cloud extinction coefficient of 30 km^{-1} were also assumed. This figure shows that the vertical partitioning of absorbed short-wave radiation is highly dependent on cloud structure.

A theoretical or even an empirical expression for solar absorption in a clear atmosphere may readily be written (Mugge and Möller, 1963; Korb and Möller, 1962; and Yamamoto, 1962), however, the expression for a cloudy atmosphere is not nearly so tenable. It is even more difficult to express a *mean* vertical partitioning of solar absorption. This can probably best be accomplished by actually measuring the short-wave divergence as a function of height. Such measurements are currently being made. In lieu of actual observations, equation (2) was adopted for the partitioning because it gave gross agreement with Davis (1963) at higher levels and assigned the

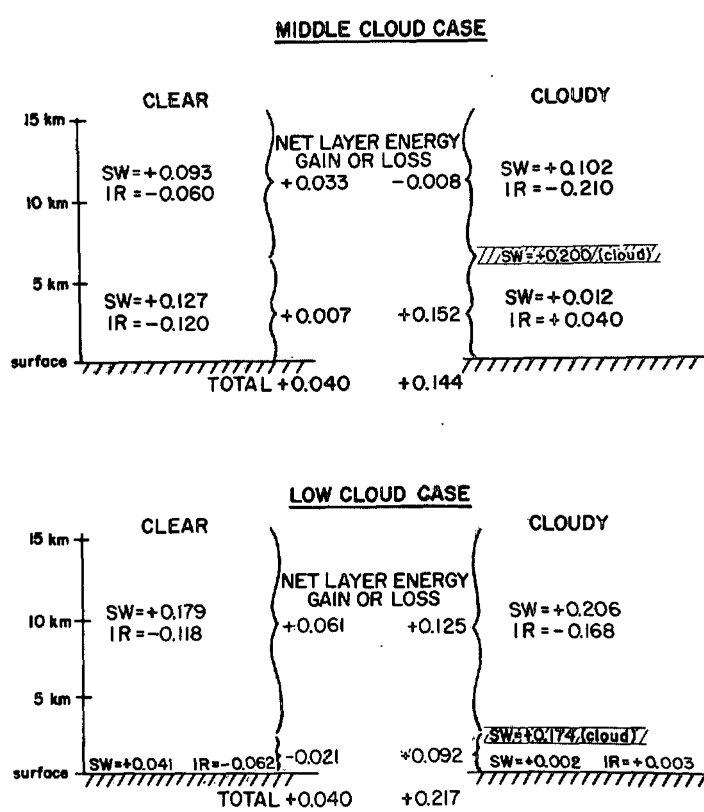

FIGURE 1.—Effects of cloud structure on the vertical distribution of short-wave absorption and total radiative balance (units: cal cm^{-2} min^{-1}).

surplus to lower layers where clouds are more likely to be present.

$$q_a = 1 - e^{-AU^*}. \qquad (2)$$

In the present study, given q_a from equation (1), equation (2) was solved for A with U^* equal to the total path length, and this value of A was used to determine q_a values for different U^* layers.

Vonder Haar (1968) has compared the results of using equations (1) and (2) with the results of Davis' short-wave technique (1963) applied to the same input data. The vertical resolution was limited to two layers, surface to 600 mb and 600 to 200 mb. The computations for the upper layer showed very good agreement while equations (1) and (2) yielded values approximately 35 percent higher than Davis' for the lower layer absorption at midlatitudes.

A direct point-by-point comparison of equation (2) with theoretical results is of limited meaning since one is comparing clear-air partitioning with *areal mean* partitioning representing many different cloud configurations. In the lowest 4 km of London's mean winter atmosphere (1957) for zero degree zenith angle, equations (1) and (2) yield 10-percent fractional solar absorption while Mugge-Möller's equation yields 9-percent and Yamamoto (1962) shows 6-percent absorption.

The solar energy absorbed was computed numerically from equation (3).

$$E = \int_{t_1}^{t_2} S \sec\theta \,(1 - e^{-AU} \sec\theta)\, dt. \qquad (3)$$

For zenith angles greater than 80°, the optical path was computed from air-mass values given in the *Smithsonian Meteorological Tables* prepared by List (1951).

Hansen derived equation (2) from data representing the fractional absorption in the entire atmospheric column, surface to the top. Since we are interested in the troposphere, we have subtracted 0.03 from the first constant in (2) to allow for absorption above 200 mb.

Given E from equation (3), the temperature change may be readily computed from (4).

$$\Delta T = \frac{g}{C_p} \frac{E}{\Delta p}. \qquad (4)$$

Theta, the solar angle, is a function of local time, the declination of the earth, and the geographical coordinates. For the solar warming models, a declination corresponding to the date March 1 was chosen. If the declination corresponding to January 1 had been used instead, the solar warming values would be decreased by approximately 25 percent.

5. RADIATION MODELS

Before attempting to interpret the synoptic radiation models, let us briefly review the effects of the distribution of clouds on radiative cooling and warming. First let us examine infrared radiative cooling. Radiative cooling is proportional to the vertical divergence of the net irradiance.

Figure 2 illustrates the effects clouds have on the radiative cooling of the atmosphere. Typical temperature and moisture distributions shown in figure 2, column a, were chosen for the calculation and different cloud structures were superimposed on these profiles. All clouds were assumed to be black.

Figure 2, column b, shows the infrared cooling in a clear atmosphere. The maximum cooling of the lower layer is accomplished by having a cloud low in the layer as in column c. The same configuration results in maximum tropospheric mean cooling. The cooling in the lower layer of column d represents a mean for the whole layer, thus it contains effects of the radiative warming beneath the cloud and the strong cooling from the cloud top. The net result is moderate cooling of the lower layer. A comparison of columns b, c, and d shows that the upper layer is virtually unaffected by the cloud structure in the lower layer. In reality there would be a slight decrease in the cooling of the upper layer as the elevation of the cloud deck beneath is increased.

A cloud at 500 mb in figure 2, column e, results in the maximum cooling of the upper layer and maximum warming of the lower layer. The extreme cooling of the upper layer is possible because most of the optical mass of water vapor is below 500 mb, and there is only a small downward radiative flux on the cloud from above.

The minimum tropospheric cooling is accomplished through configuration in figure 2, column f. A cloud high in the troposphere acts as a "lid" and does not allow the atmosphere to cool effectively.

The final configuration, figure 2 (column g), shows the effect of multilayer clouds. There is relatively small cooling in the lower layer with significant cooling off the top of the upper layer cloud and thus of the upper layer itself.

Water vapor and clouds are the primary variables modulating direct solar absorption. As the optical mass of water vapor increases, so does the solar absorption. High clouds above most of the atmosphere's water vapor tend to decrease solar absorption by reflecting energy back to space before it encounters an appreciable optical mass of water vapor, and low clouds tend to increase the absorption by reflecting solar energy through a longer path length of water vapor and other absorbers.

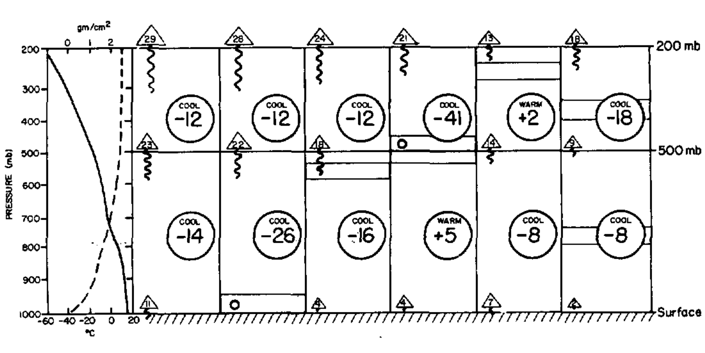

FIGURE 2.—Effects of cloud distribution on infrared cooling. The dashed line in column a is cumulative precipitable water (gm/cm²); the solid line is temperature (°C). The arrows represent net radiation (ly min$^{-1}\times 100$) and the circles represent the mean infrared radiative temperature change (°C day$^{-1}\times 10$) of the layer. Shaded areas depict the presence of clouds which were assumed to be black (emissivity = 1.0).

The short-wave data in figure 1 are taken from Korb and Möller (1962), and the long-wave data from calculations assuming black clouds. The (SW) numbers refer to absorbed short-wave energy in the bracketed layer in units of cal cm^{-2} min^{-1}. The (IR) numbers refer to net infrared loss of energy in cal cm^{-2} min^{-1} from the bracketed layer. Figure 1 shows that despite the decrease of short-wave absorption in the subcloud layer, a marked net warming occurs beneath the cloud in both the low and middle cloud cases. This warming is due primarily to the infrared term and may be enhanced by adding the cloud-absorbed short-wave energy to the subcloud layer's net gain.

The most striking feature of figures 1 and 2 is how clouds act to increase the warming of the atmosphere by both short-wave absorption and infrared radiation convergence. In the daytime with high incident solar radiation, low clouds represent the most efficient configuration for tropospheric warming. At night, a high dense cloud represents a more effective warming configuration. Unfortunately there is insufficient data available to say exactly what effects cirrus clouds will have on short-wave warming of the troposphere; however, it is doubtful that the optimum configurations outlined above would change.

The synoptic radiation models given in figures 4 through 15 are centered at ϕ_0 and λ_0, 40° N. latitude and 95° W. longitude, respectively. The grid is meant as a relative distance scale and not to imply that the model is appropriate only to synoptic features centered at 40° N., 95° W. As was mentioned previously, most of the radiation data were collected from Green Bay, Wis., and Sterling, Va., and thus represent continental rather than maritime conditions.

The infrared cooling and short-wave warming are depicted in four different ways for each synoptic system. Figures 6, 7, 10, and 11 show isopleths of mean radiative temperature change for the two layers, surface to 500 mb and 500 to 200 mb. Figures 5, 8, 9, 12, and 13 give mean radiative temperature changes for both radiative components and their sum for each 100-mb layer in the four quadrants defined by:

$$\text{quadrant I } \phi>\phi_0,\ \lambda<\lambda_0,$$

$$\text{quadrant II } \phi>\phi_0,\ \lambda>\lambda_0,$$

$$\text{quadrant III } \phi<\phi_0,\ \lambda>\lambda_0, \text{ and}$$

$$\text{quadrant IV } \phi\leq\phi_0,\ \lambda\leq\lambda_0.$$

Table 1 is a summary of regional, mean radiative temperature changes, their standard deviations, and the number of data points for the surface–500-mb and 500–200-mb layers.

Table 2 represents a statistical summary of the difference in the mean radiative temperature change between the surface–500-mb layer and the 500–200-mb layer. This presentation is made to illustrate if, and to what extent, the vertical distribution of the radiative components act to destabilize the atmosphere. For example, diabatic cooling of a higher layer relative to a lower layer would decrease the static stability of the region. The distribution of the differences of mean radiative temperature changes approximates a normal distribution; thus we may estimate the probability of occurrence of a given destabilization rate from the appropriate area under the curve in figure 3. Columns 3 and 4 in table 2 represent the probability of occurrence of a radiative destabilization tendency and a tendency less than -1°C day^{-1}, respectively. All statistics are computed from the raw, unsmoothed data.

The four formats depicting each synoptic feature were chosen to give as complete a description of the radiative characteristics as possible. A comprehensive text referring to all the characteristics of the radiative patterns is beyond the limits of reasonable length; therefore, only the most significant features will be pointed out.

The stationary front, in figures 4 and 5 and table 1, shows significantly less IR cooling in the lower layers in quadrant I than in quadrant IV. The SW warming in the lower layer in quadrant IV causes net warming relative to the upper layer. Table 2 shows that both quadrants have a tendency toward radiation destabilization, the upper layer cooling 1.14°C day^{-1} relative to the lower in quadrant I and 0.68°C day^{-1} in quadrant IV. The probability that the upper layer will cool more than the lower is 0.73, second highest of all cases examined.

The nascent cyclone, figures 6 and 8, shows significant variations in both radiative components. An area of minimum IR cooling and maximum SW warming is apparent in quadrant IV. This contrasts to a near-maximum IR cooling in the surface–500-mb layer and a minimum SW warming in quadrant II. Quadrant II also shows the smallest standard deviation in the IR component in table 1 for the lower layer, 0.36°C day^{-1}, while quadrant II is most uniform in the upper layer. Unfortunately there were only three ascents in this sector of the storm, so one must be cautious about making any general conclusions from this quadrant. At the other extreme for the lower layer are quadrants I and II with standard deviations equal to 0.89°C day^{-1}, and quadrant IV with a standard deviation of 1.95°C day^{-1} for the 500–200-mb layer. Table 2 shows that quadrants I and II have a mean tendency to destabilize, while the remaining two quadrants have the opposite tendency. Most significant for quadrants II, III, and IV are the large standard deviations, indicating a large range of variation of radiative destabilization. The probability of a destabilization tendency is approximately 0.5 for all four quadrants.

Figures 7 and 9 represent the warm sector cyclone model. The two northern quadrants have larger IR cooling rates in the 500–200-mb layer and smaller cooling rates in the surface–500-mb layer than quadrants III and IV. In table 1, quadrant III shows a large degree of uniformity in the infrared patterns with standard deviations of 0.54 and 0.47°C day^{-1} for the surface–500- and 500–200-mb layers, respectively. The two most significant SW features are the 0.99°C day^{-1} maximum in quadrant III and the remarkably uniform surface–500-mb layer in quadrant I with a standard deviation of 0.19°C day^{-1}.

Table 2 shows that all four gradrants have mean destabilization tendencies: values in quadrants II, III, and

TABLE 1.—*Statistical summary of the surface—500-mb and 500—200-mb radiative temperature changes (°C day⁻¹)*

	Quadrant I ($\phi>\phi_0$, $\lambda<\lambda_0$)			Quadrant II ($\phi>\phi_0$, $\lambda>\lambda_0$)			Quadrant III ($\phi<\phi_0$, $\lambda>\lambda_0$)			Quadrant IV ($\phi\leq\phi_0$, $\lambda\leq\lambda_0$)		
	Mean	Std. dev.	No.	Mean	Std. dev.	No.	Mean	Std. dev.	No.	Mean	Std. dev.	No.
STATIONARY FRONT												
Infrared model:												
SFC-500 mb	−0.73	0.99	5							−1.80	0.72	12
500-200 mb	−1.32	.93	5							−1.13	.85	12
Short-wave model:												
SFC-500 mb	.68	.32	5							1.03	.33	12
500-200 mb	.12	.06	5							.15	.11	12
Sum (IR+SW):												
SFC-500 mb	−.05	1.01	5							−.78	.68	12
500-200 mb	−1.20	.92	5							−1.00	.85	12
NASCENT CYCLONE												
Infrared model:												
SFC-500 mb	−1.41	.89	22	−2.18	0.89	3	−2.19	0.36	13	−1.68	.68	22
500-200 mb	−.95	1.13	22	−.71	.40	3	−.93	.65	13	−.47	1.95	22
Short-wave model:												
SFC-500 mb	.71	.46	24	.67	.62	3	.79	.41	15	.82	.39	24
500-200 mb	.09	.11	24	.04	.04	3	.08	.06	15	.12	.08	24
Sum (IR+SW):												
SFC-500 mb	−.70	.95	22	−1.51	.36	3	−1.40	.20	13	−.88	.76	22
500-200 mb	−.86	1.10	22	−.67	.37	3	−.84	.61	13	−.33	1.99	22
WARM SECTOR CYCLONE												
Infrared model:												
SFC-500 mb	−1.18	.86	29	−1.42	.80	26	−1.72	.54	15	−1.80	1.31	16
500-200 mb	−1.45	.93	29	−1.46	.68	26	−1.23	.47	15	−1.03	.76	16
Short-wave model:												
SFC-500 mb	.68	.19	12	.67	.34	8	.82	.44	9	.99	.41	9
500-200 mb	.07	.06	12	.09	.04	8	.07	.06	9	.12	.07	9
Sum (IR+SW):												
SFC-500 mb	−.83	.65	12	−.49	.72	8	−1.15	.68	9	−1.07	.77	7
500-200 mb	−1.13	.70	12	−1.24	.75	8	−.86	.44	9	−.81	.70	7
OCCLUDED CYCLONE												
Infrared model:												
SFC-500 mb	−1.62	.67	18	−1.13	.53	3	−1.99	.60	17	−1.91	.51	14
500-200 mb	−1.13	.79	18	−.67	.17	3	−.87	.58	17	−1.03	.44	14
Short-wave model:												
SFC-500 mb	.71	.43	19	.45	.15	3	.56	.29	19	1.18	.37	15
500-200 mb	.10	.12	19	.06	.01	3	.04	.02	19	.18	.09	15
Sum (IR+SW):												
SFC-500 mb	−.94	.78	18	−.68	.43	3	−1.41	.71	17	−.78	.65	14
500-200 mb	−1.02	.76	18	−.61	.18	3	−.86	.59	17	−.87	.45	14
ANTICYCLONE												
Infrared model:												
SFC-500 mb	−1.82	.66	33	−1.73	.56	18	−1.28	.89	15	−1.85	.61	42
500-200 mb	−.89	.58	33	−1.27	.72	18	−1.20	.61	15	−.98	.61	42
Short-wave model:												
SFC-500 mb	.51	.32	37	.71	.36	20	.83	.45	17	.67	.36	43
500-200 mb	.06	.06	37	.10	.08	20	.13	.16	17	.06	.05	43
Sum (IR+SW):												
SFC-500 mb	−1.32	.65	33	−1.06	.55	18	−.43	1.00	15	−1.17	.61	42
500-200 mb	−.82	.58	33	−1.20	.70	18	−1.06	.58	15	−.93	.60	42

IV are especially extreme, −1.21, −0.92, and −0.79°C /day, respectively. The standard deviations are not correspondingly large for quadrants II, III, and IV, and the probabilities of occurrence of destabilization tendencies are 0.78, 0.58, and 0.62, respectively.

The occluded cyclone model shown in figures 10 and 12 shows the maximum observed SW absorption in quadrant IV. In the opposite sense, quadrant II shows a minimum value of SW warming, probably due to the southward invasion of cold, dry, continental air. However, the few soundings available for analysis in this quadrant limits our confidence in these values. Table 2 shows that quadrants I and II have a mean tendency toward radiative destabilization, while III and IV tend to be stabilized by the vertical distribution of the radiative components.

The anticyclone model in figures 11 and 13 shows the anticyclone's classic uniformity. There is relatively little contrast between the radiative components from one quadrant to another. Quadrants II and III do have slightly larger SW warming caused by the moisture-laden air entering the circulation from the southwest. The exact opposite argument, dry continental air from the north, accounts for the smaller SW warming in quadrants I and IV. All four quadrants show a mean tendency toward radiative stabilization in table 2, with quadrant III having the most variation.

6. A COMPARISON OF HEATING TERMS

Converting the radiative cooling and warming rates into thickness tendencies using the hypsometric equation provides a convenient "scale" with which to assess potential radiative effects. Such a step is of course a gross oversimplification, since it assumes that all the energy exchanged by radiative processes results directly in temperature or thickness changes. In reality, there are complicated interactions between radiation processes, latent heating, sensible heat transfer, and vertical motions.

In spite of the simplification induced by assuming the atmosphere would actually cool (contract) and warm (expand) directly from radiative transfer, it is instructive to compare these radiative thickness tendencies with thickness tendencies due to other terms in a themodynamic energy equation.

TABLE 2.—*Statistical summary of the difference between the mean radiative temperature changes (°C day⁻¹) of the surface-500-mb layer and the 500–200-mb layer*

	(1) Mean	(2) Standard deviation	(3) Percent area of destabilization under normal curve	(4) Percent area of destabilization ≥−1°C day⁻¹ under normal curve	(5) Number of observations
Stationary front					
Quadrant I	−1.14	1.83	73	53	5
Quadrant IV	−.68	1.71	65	42	12
Nascent cyclone					
Quadrant I	−.16	1.34	55	26	22
Quadrant II	−.44	4.66	53	45	3
Quadrant III	.22	3.95	48	38	13
Quadrant IV	.61	2.86	42	29	22
Warm sector cyclone					
Quadrant I	−.30	1.05	61	26	12
Quadrant II	−1.21	1.57	78	55	8
Quadrant III	−.92	2.00	58	35	9
Quadrant IV	−.79	2.59	62	42	7
Occluded cyclone					
Quadrant I	−.08	1.30	52	24	18
Quadrant II	−.39	3.78	54	44	3
Quadrant III	.49	1.78	39	47	17
Quadrant IV	.50	2.16	41	25	14
Anticyclone					
Quadrant I	.50	1.01	31	07	33
Quadrant II	.79	1.74	34	15	18
Quadrant III	.32	2.58	45	31	15
Quadrant IV	.36	1.79	42	23	42

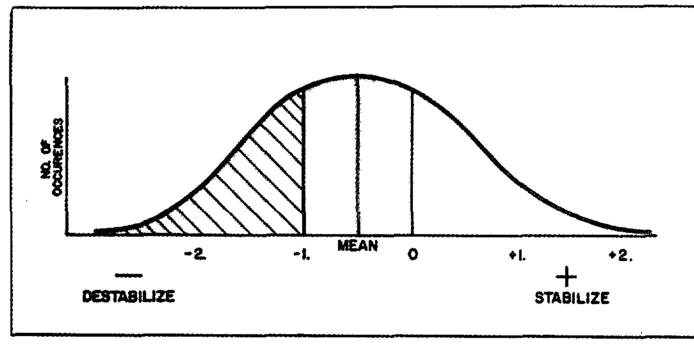

FIGURE 3.—Assumed normal distribution curve of difference in mean net radiative temperature change (°C/day) for the surface-500-mb and 500–200-mb layers. Shaded area corresponds to probability of radiative destabilization tendency and crosshatched area to the probability that a destabilization tendency ≥ −1°C/day will be observed.

Four synoptic situations analyzed by Petterssen et al. (1962) were selected for this comparison. Petterssen numerically evaluated, for the 1000–500-mb layer, the 3-hr thickness tendency due to dry adiabatic motion, sensible heating, and latent heating. They added the three-thickness tendency components to the original thickness field and compared the result to the observed thickness field. In this study, the two radiative components, short-wave warming and infrared cooling, have been added to Petterssen's results.

The radiation models in figures 6, 7, 10, and 11 were subjected to the inverse of the gridding procedure outlines in section 2 so that the position of the fronts in the actual synoptic situation defined the orientation of the radiation patterns. Since short-wave absorption is strongly

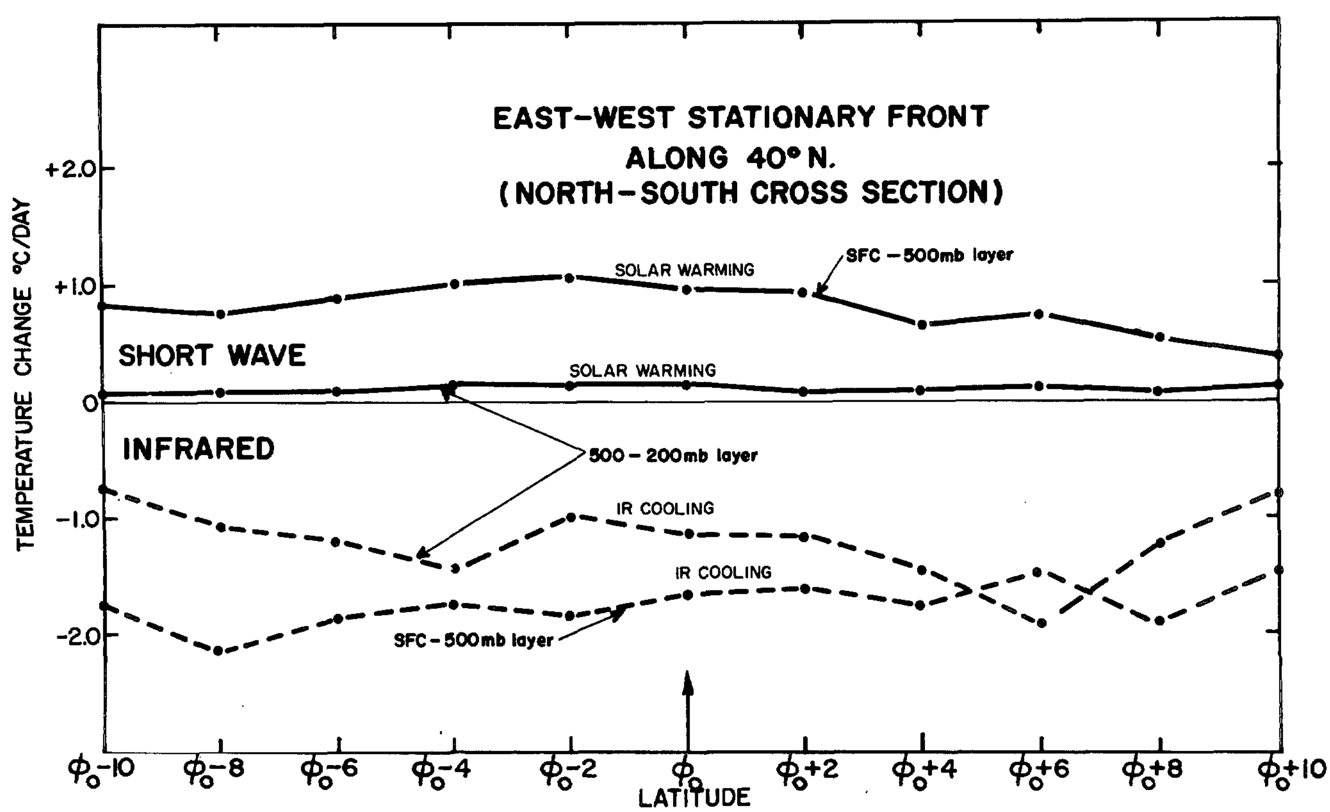

FIGURE 4.—Stationary front radiative temperature change (°C day⁻¹) model for surface–500-mb and 500–200-mb layers.

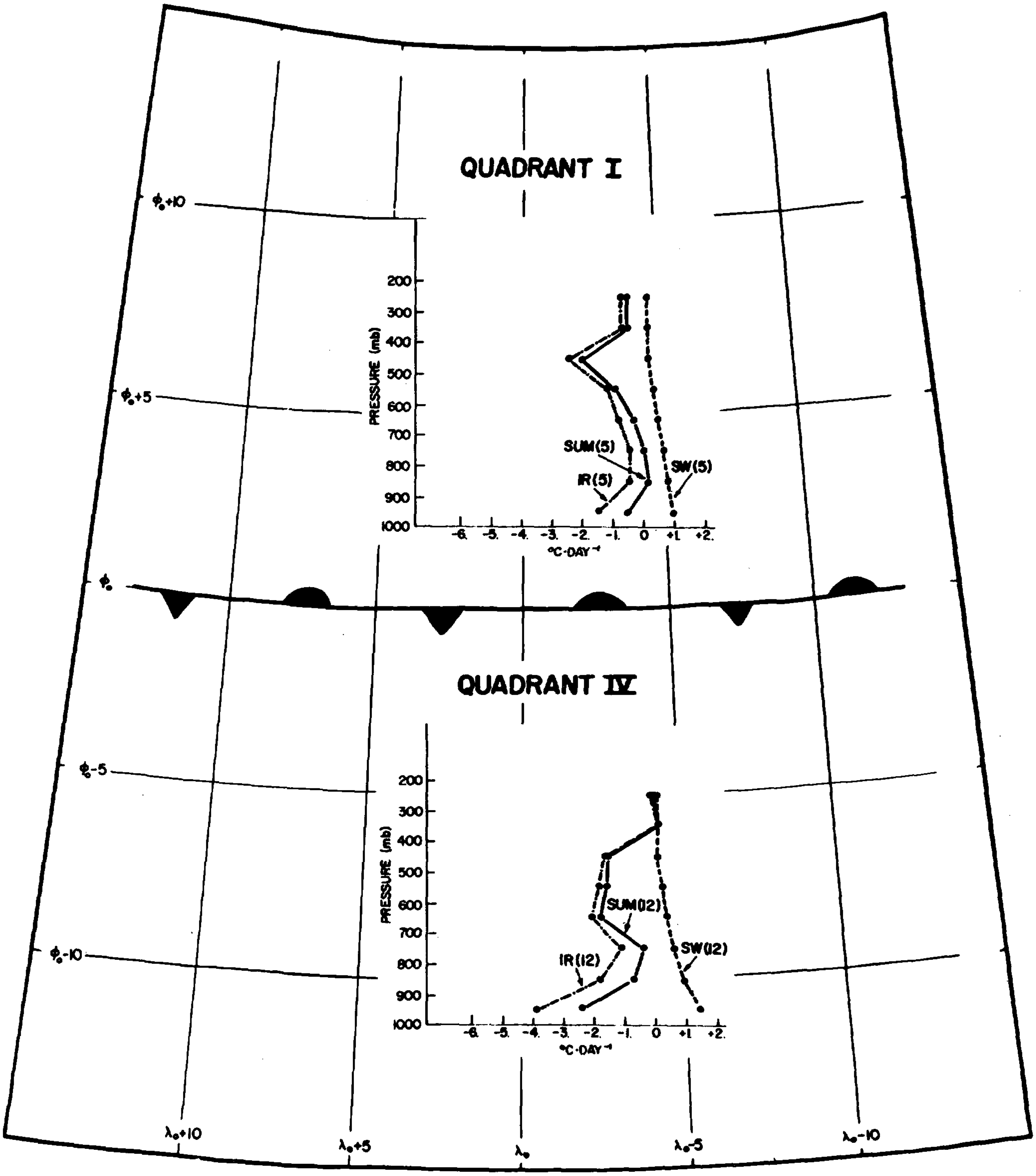

FIGURE 5.—Stationary front radiative temperature change (°C day⁻¹) summary for 100-mb layers. (Numbers in parentheses represent the number of data points.)

dependent on solar zenith angle, the short-wave component was computed by numerically integrating equation (3) for the actual 3-hr period. If one wishes to extend the interpretations of figures 9–12 for periods longer than 3 hr, he must take into account the strong time dependence of the short-wave term, while the infrared term is virtually independent of local time.

There is a significant geographical difference between the locations of Petterssen's North Atlantic analyses and the data from Green Bay, Wis., and Sterling, Va., from which the radiation models were derived. The difference is basically meridional, not latitudinal; therefore, we are still considering the same type of synoptic features. The primary difference in radiative characteristics is apt to be caused by effects from the underlying surface, continent versus ocean.

In section 5, the cloud structure was assumed to be the primary variable modulating the radiation cooling.

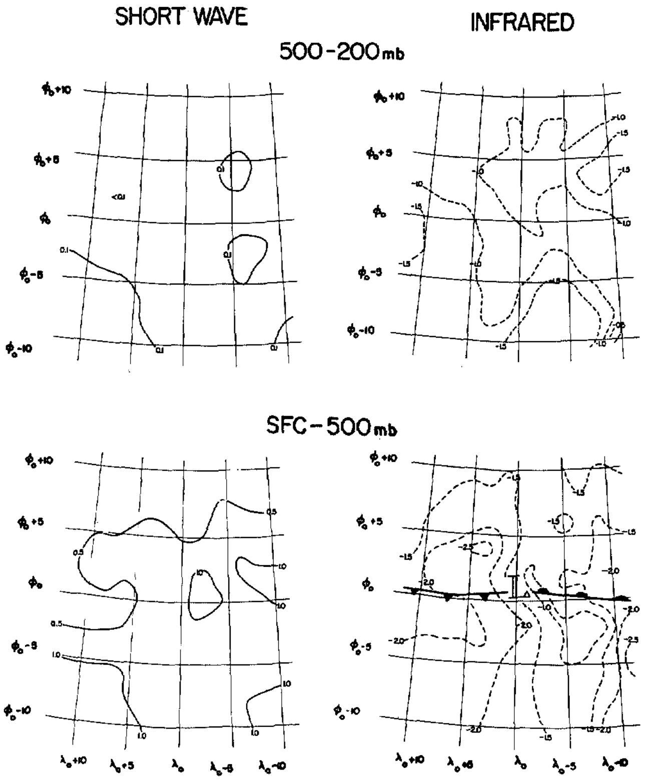

FIGURE 6.—Nascent cyclone radiative temperature change (°C day^{-1}) model for surface–500-mb and 500–200-mb layers.

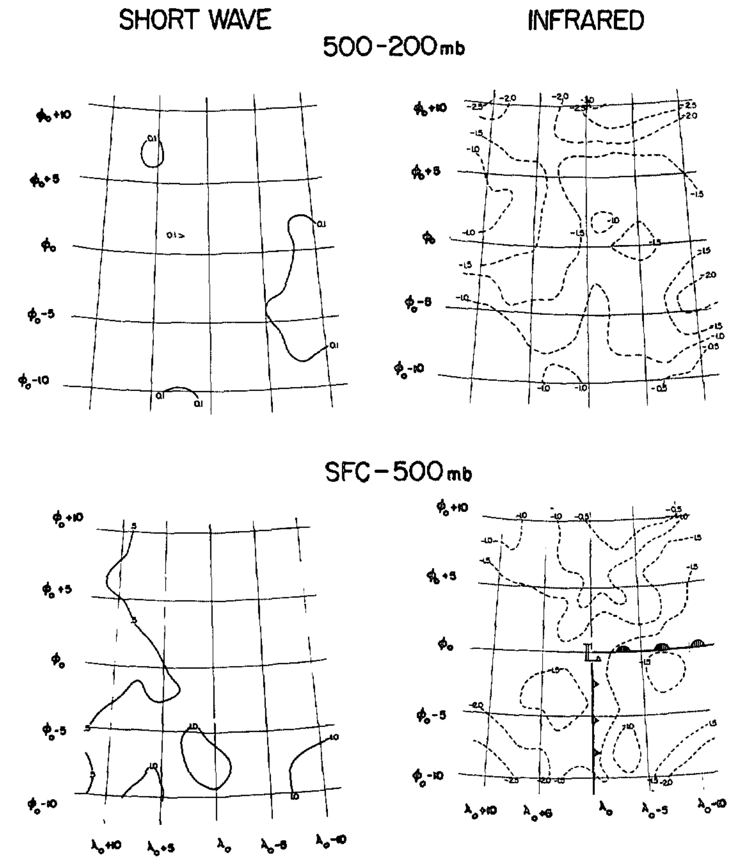

FIGURE 7.—Warm sector cyclone radiative temperature change (°C day^{-1}) model for surface–500- and 500–200-mb layers.

Within the resolution of our analyses, this remains a good assumption. For the purpose of comparing the radiative thickness tendency components to other thermodynamic processes, the cloud structure is assumed to be the same for both continental and maritime systems, although this assumption may not be rigorously correct. For the short-wave warming, water vapor assumes the role of principal modulator. Sterling, Va., soundings often represent maritime Atlantic upper air conditions. Since approximately one-half of the data used in this study was collected from Sterling, there is in the models a built-in maritime effect.

Figures 14, 15, 16, and 17 illustrate one point very well. The radiative terms are *not* negligibly small compared to other terms, even for a time period as small as 3 hr. Besides the magnitude of the radiative components, one must consider the gradient and organization of the thickness tendency. In the nascent cyclone case, figure 14, a difference of 15 ft/3 hr exists in the east-west direction in both the infrared and short-wave components. Even more striking is the fact that the differences are of like sign, so when the terms are added, a 30 ft/3 hr net difference exists. The implications of this organization on cyclone development are discussed in the next section.

The infrared cooling minimum in figure 14 is closely alined with the latent heat maximum, while the solar warming maximum is displaced farther south and east in the warm sector. The infrared cooling maximum and short-wave minimum are behind the cold front in the dry, cold air where the sensible heat transfer is a maximum.

Analyses G, H, and I enable one to compare the 3-hr forecasts, with and without radiation, to the observed tendency. An initial glance at G and H serves to verify that the inclusion of radiation does not dramatically change the thickness pattern. However, closer inspection reveals that the infrared cooling west of the low center causes a larger shrinking of the layer in that region, and the resulting thickness field is more nearly that of the observed. This same cooling accounts for the eastward deflection of the zero contour, although it is not sufficient to agree perfectly with the observed case. The short-wave warming maximum in the warm sector makes the area of positive thickness change larger than the observed.

Figure 15, the warm sector cyclone, shows a relative minimum of infrared cooling associated with the latent heat term, though the radiation patterns are not as distinctive as in the nascent case. The absolute minimum of infrared cooling occurs in an area where convective clouds would produce precipitation and most probably cirrus at high levels. Petterssen did not include effects of convection in this analysis; however, if he had, one can be fairly certain of a positive latent heating contribution in this area. The solar term follows the characteristic cyclone moisture patterns, a moist warm sector and drier air to the northwest.

The infrared and short-wave terms quite effectively cancel one another when added together. However, in the

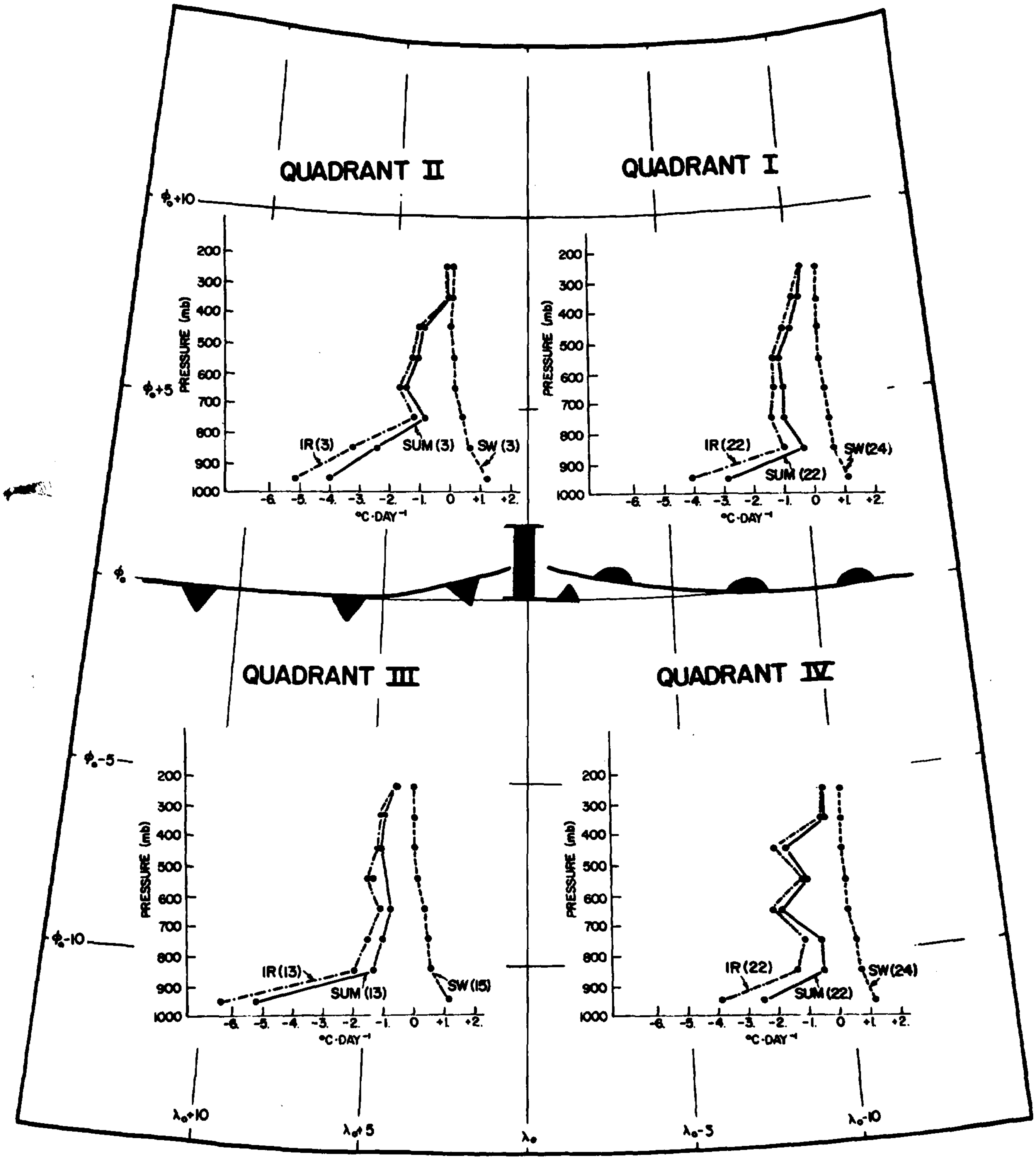

FIGURE 8.—Nascent cyclone radiative temperature change (°C day^{-1}) summary for 100-mb layers. (Numbers in parentheses represent the number of data points.)

far northwest corner the infrared term dominates and results in a net radiation thickness change of −10 ft/3 hr, while south of the low center the solar term prevails resulting in a +5 to 10 ft/3 hr net radiative thickness change. The addition of the radiative terms results in only small differences between G and H. It should be noted that in both the nascent and warm sector cases, the adiabatic term dominates the thickness tendency field.

The occluded cyclone case, figure 16, shows less correlation between the radiation patterns and the other components than did figures 14 and 15. The latent heat maximum really shows no corresponding feature in either of the radiation components. However, the radiation features do appear to correspond to air-mass type. The maximum infrared cooling occurs behind the point of occlusion at approximately the same point where a dry

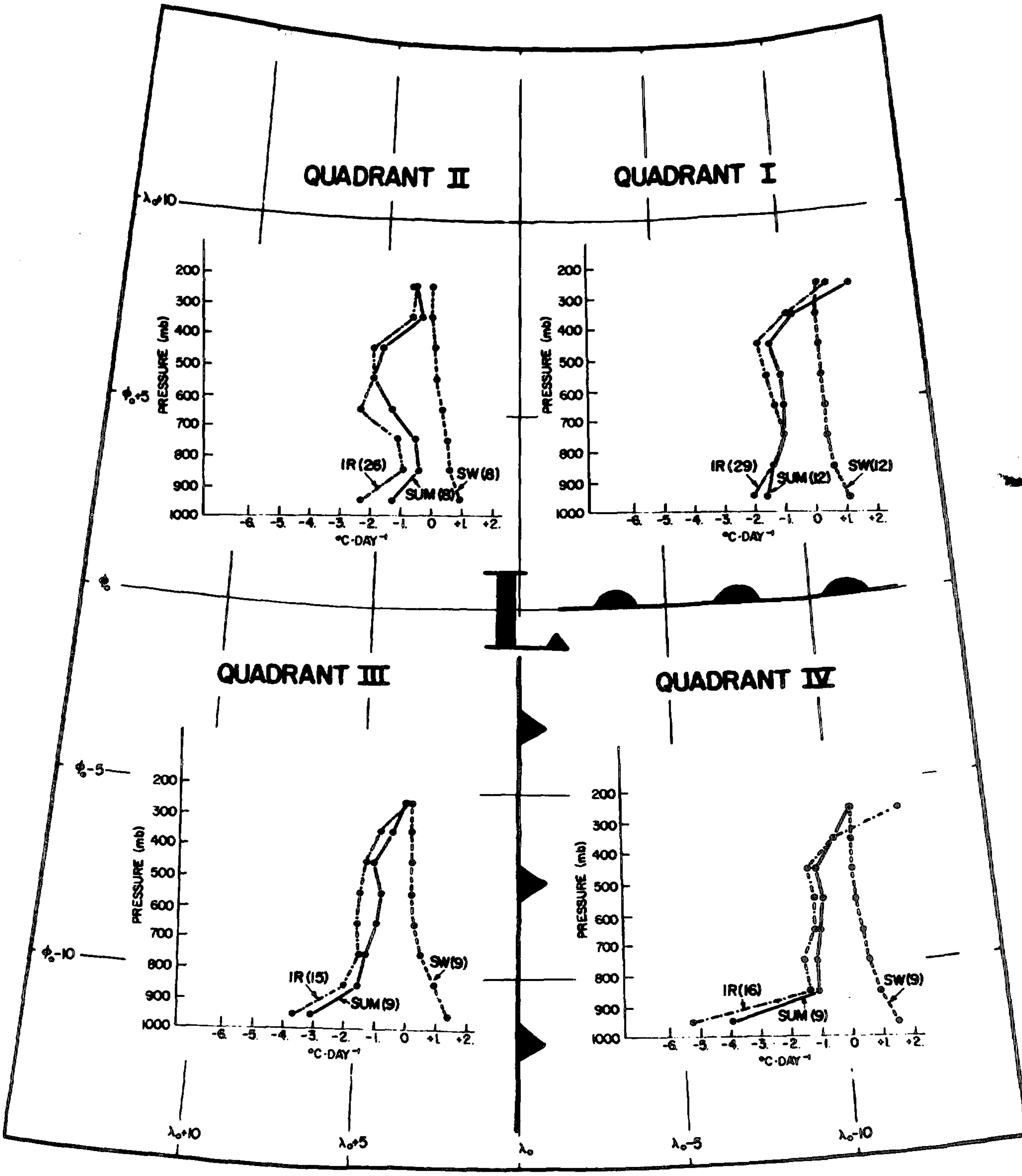

FIGURE 9.—Warm sector cyclone radiative temperature change (°C day^{-1}) summary for 100-mb layers. (Numbers in parentheses represent the number of data points.)

trough appears on the short-wave analysis. In front of and alined with the occluded front, the infrared component decreases, indicating higher clouds ahead of the front. Coinciding with this decrease in infrared cooling is a ridge of short-wave warming.

A comparison of G and H with I in figure 16 shows improvement from the inclusion of radiative terms everywhere except in the northeast quadrant. The radiation components displace the zero isoline farther east and enlarge the area of negative thickness tendency. This gives better agreement between the observed and calculated analyses. However, this same tendency toward negative values results in a decrease in values in the northeast quadrant of H; therefore, ahead of the occluded front, the radiation components produced greater disagreement between the computed and observed analyses.

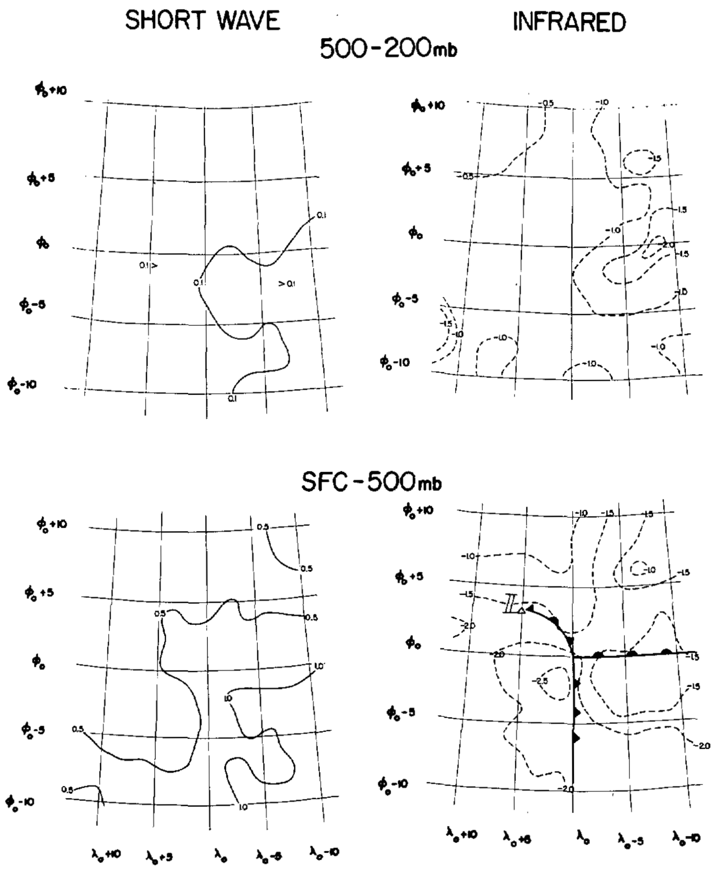

FIGURE 10.—Occluded cyclone radiative temperature change (°C day^{-1}) model for surface–500- and 500–200-mb layers.

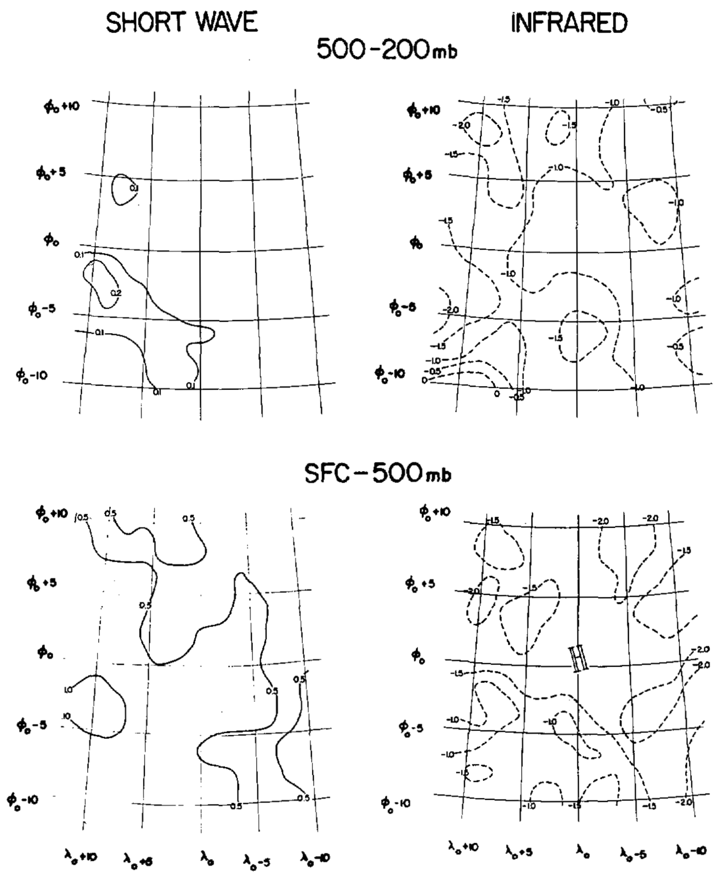

FIGURE 11.—Anticyclone radiative temperature change (°C day^{-1}) model for surface–500-mb and 500–200-mb layers.

The anticyclone case in figure 17 shows comparatively little horizontal contrast in either radiative component. The two components are also of like magnitude and opposite sign. As a result, their inclusion has a relatively small effect on the analysis. However, an improvement does occur at the point of the maximum observed thickness tendency which is decreased by a ridge of infrared cooling on the east side of the anticyclone.

Table 3 lists the extreme values of the thickness contours of each component for all four synoptic cases. From this table one readily sees that the adiabatic term is the largest for all four cases. However, of particular interest to us is the magnitude of the radiative terms relative to the total thickness change. For the nascent case the short-wave and infrared maxima are 25 percent of the maximum observed thickness change. The radiative component maxima are both 10 percent of the observed maximum for the warm sector case; the infrared and short wave are 25 percent and 19 percent, respectively, of the observed maximum tendency for the occluded case and 33 percent for the anticylcone. It is also interesting to note that the sensible heat and latent heat transfer terms have magnitudes directly comparable to the radiative terms.

7. RADIATIVE CONTRIBUTION TO VORTICITY

Petterssen (1956) has derived equation (5) which related the Laplacian of the thickness tendency for the layer, surface to the level of nondivergence, to the vorticity change at the surface.

$$\frac{dQ_0}{dt}=\mathbf{V}\cdot\nabla Q+\mathbf{V}_0\cdot\nabla Q_0-\frac{g}{f}\nabla^2\overline{(\mathbf{V}\cdot\nabla T)}-\frac{R}{f}\nabla^2\left(\log\left(\frac{p}{p_0}\right)\overline{\omega(\Gamma_d-\Gamma)}\right)-\frac{R}{fc_p}\nabla^2\left(\log\left(\frac{p}{p_0}\right)\overline{\frac{dH}{dt}}\right). \quad (5)$$

The total observed vorticity change, the left side of (5), has been observed to be of the order 10^{-9} to 10^{-10} sec^{-2} (Panofsky, 1956).

In order to assess the effects of radiation on the vorticity field, let us assume the u, v, and w components of velocity are zero. Then all terms on the right-hand side of (5) vanish except the last term representing the diabatic thickness tendency. The Laplacians of the infrared cooling and short-wave warming fields for the surface–500-mb layer in figures 6, 7, 10, and 11 are computed from a 2° latitude by 2° longitude grid in order to establish the vorticity change due to the radiative components. Table 4 presents the mean vorticity change over the entire model area induced by the two radiation components.

In this crude assessment of the vorticity production by radiation, the exact vertical partitioning method for solar absorption is not critical. The partitioning methods will differ mainly in the detailed vertical structure and not in the gross, 500-mb-thick layer used in this computation.

The nascent cyclone case shows the most significant feature in table 4. The two radiative components combine

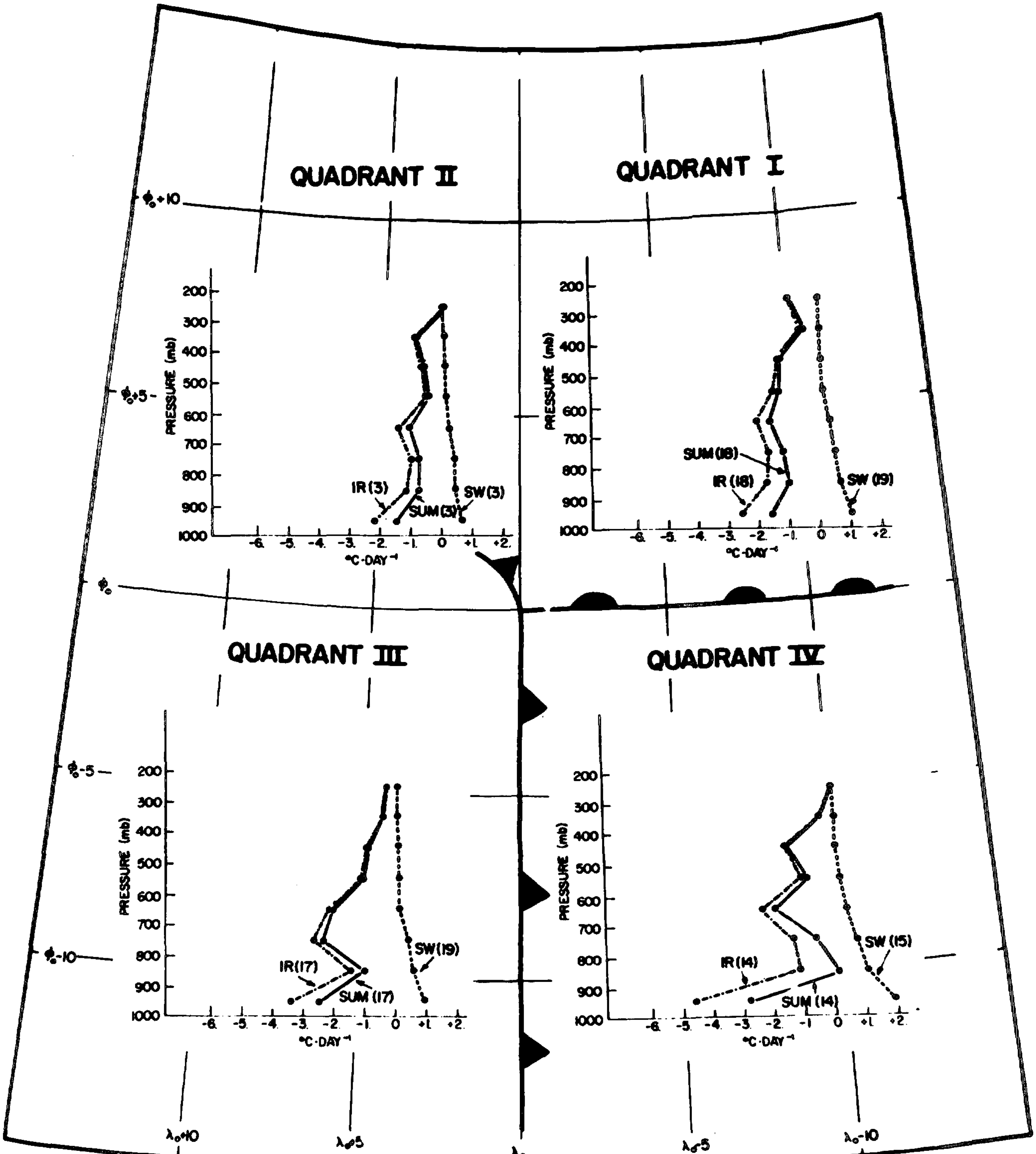

FIGURE 12.—Occluded cyclone radiative temperature change (°C day^{-1}) summary for 100-mb layers. (Numbers in parentheses represent the number of data points.)

to give a vorticity tendency of 6×10^{-10} sec^{-2}. Such a large component of vorticity change is comparable to the expected total vorticity change. The short-wave component accounts for approximately three times as much vorticity production as the infrared term.

The warm sector case shows positive vorticity production from both radiation terms, however, about five times smaller than for the nascent stage.

In the occluded cyclone, the organization of the short-wave warming produces a significant negative vorticity tendency component while the infrared term is positive but comparatively small. The occluded cyclone is the only case where the net radiative effect is to decrease the vorticity.

The anticyclone weakens, or gains cyclonic vorticity, from the net radiative contribution. The short-wave

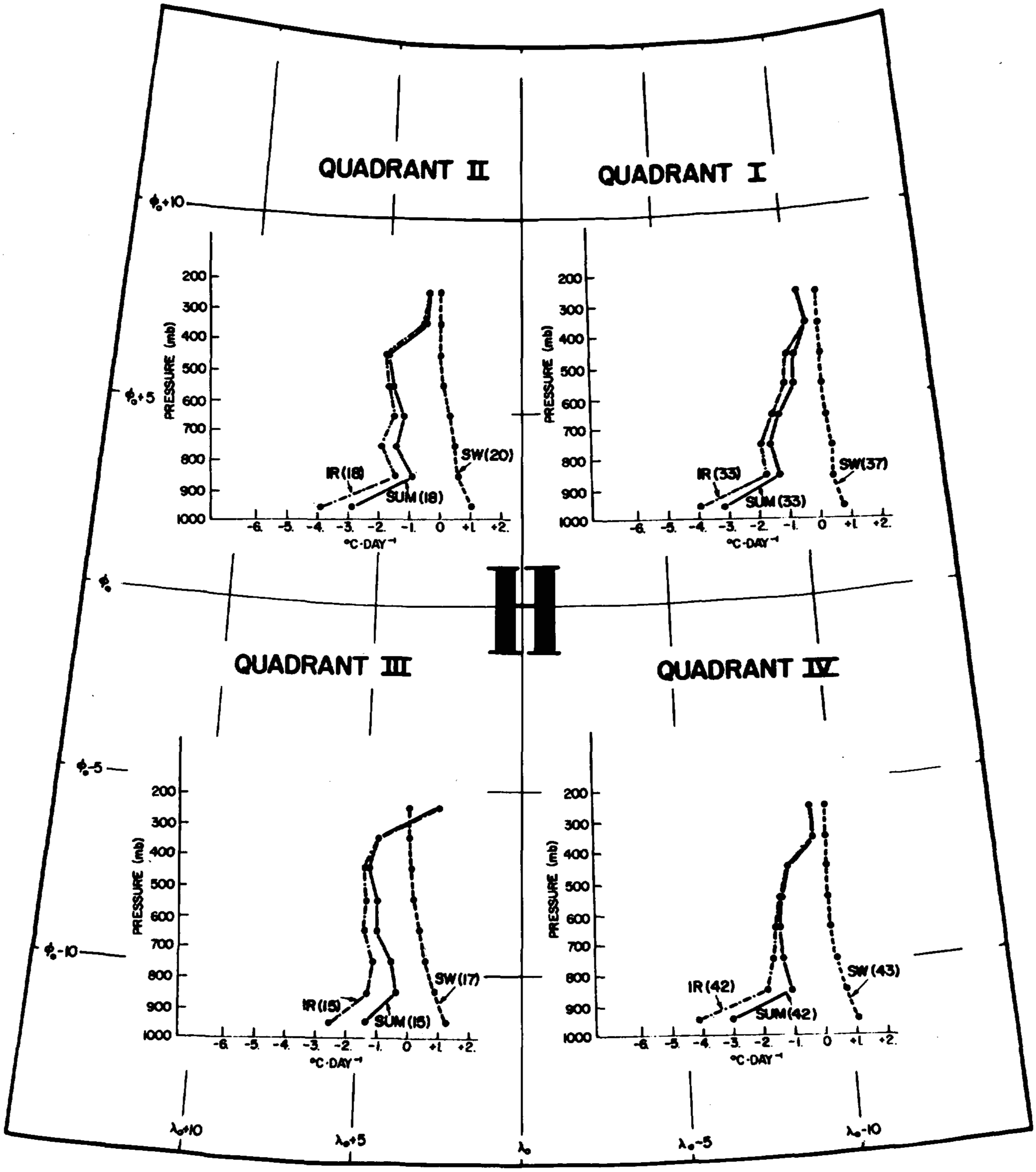

FIGURE 13.—Anticyclone radiative temperature change (°C day^{-1}) summary for 100-mb layers. (Numbers in parentheses represent the number of data points.)

component is negative but smaller by a factor of 7 than the positive infrared component.

8. CONCLUSIONS

Infrared and short-wave radiation processes may be significant contributors to synoptic scale development. In the simplified thickness tendency approach used in this research, the magnitude of the vorticity change attributable to radiative processes is 6×10^{-10} sec^{-2} for the nascent cyclone case. This compares with total expected change of 10^{-9} to 10^{-10} sec^{-2}. The radiative contributions for other synoptic features are smaller by a factor of approximately 6. The nascent, warm sector, and anticyclone cases show positive cyclonic development from radiation components, while the occluded cyclone shows a production of anticyclonic vorticity.

Inclusion of radiative components in 3-hr-thickness tendency analyses shows that radiative component

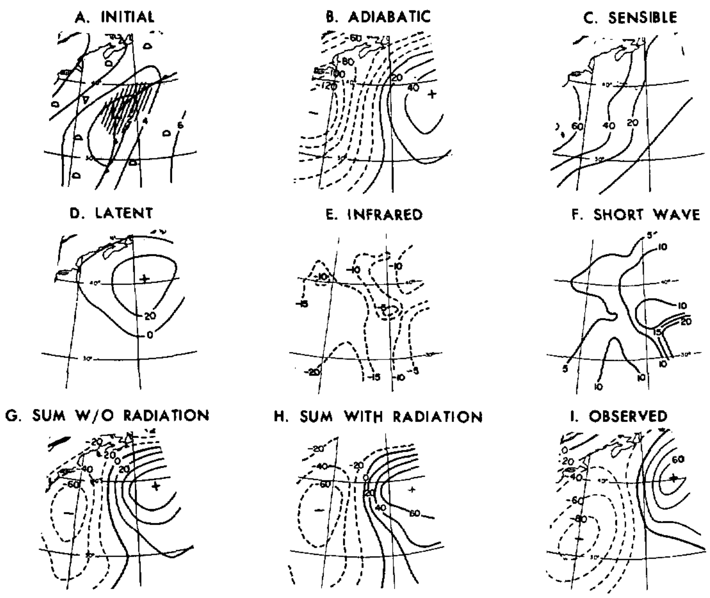

FIGURE 14.—Computation of 3-hr thickness change of 1000–500-mb layer, nascent cyclone case (1200 GMT, Jan. 4, 1958). (A) 1000-mb surface (hundreds of feet); (B) thickness change (ft/3 hr) due to adiabatic motion; (C) thickness change due to sensible heat flux from the surface; (D) thickness change due to release of latent heat; (E) thickness change due to infrared cooling; (F) thickness change due to short-wave warming; (G) sum of B, C, and D; (H) sum of B, C, D, E, and F; (I) observed thickness change. (Analyses A, B, C, D, G, and I taken from Petterssen et al., 1962.)

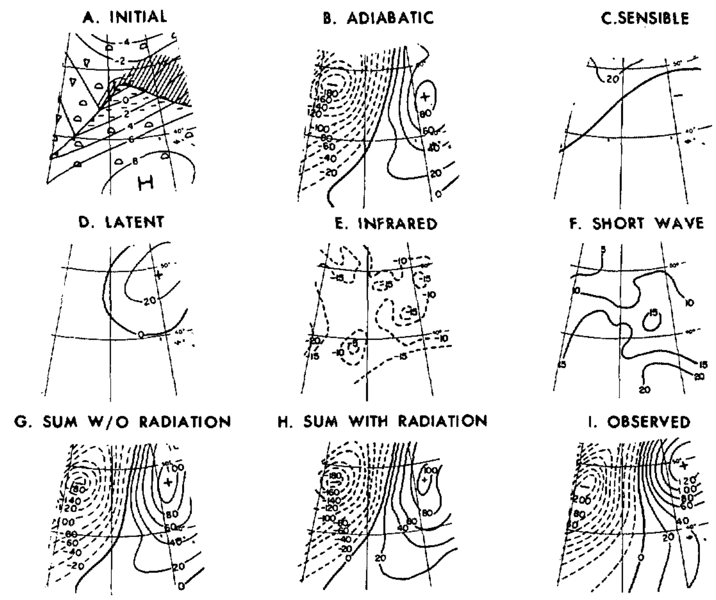

FIGURE 15.—Computation of 3-hr thickness change of 1000–500-mb layer, warm sector cyclone case (1200 GMT, Jan. 5, 1958). (A) 1000-mb surface (hundreds of feet); (B) thickness change (ft/3 hr) due to adiabatic motion; (C) thickness change due to sensible heat flux from the surface; (D) thickness change due to release of latent heat; (E) thickness change due to infrared cooling; (F) thickness change due to short-wave warming; (G) sum of B, C, and D; (H) sum of B, C, D, E, and F; (I) observed thickness change. (Analyses A, B, C, D, G, and I taken from Petterssen et al., 1962.)

maxima are 10–33 percent of the observed maximum values of the total thickness change. The radiative components are of the same order of magnitude as the latent and the sensible heat terms and correlate well with air mass and cloud organization associated with classical midlatitude synoptic systems.

ACKNOWLEDGMENTS

I would like to express my gratitude to the Environmental Science Services Administration (ESSA) for their support of the research reported in this paper through Grant E 22-113-68 (G). Also instrumental in this research were the Weather Bureau upper air stations responsible for the gathering of the data. ESSA personnel in the IQSY radiation project working with Dr. Peter Kuhn reduced and made the radiometer data available. Mr. Terry Yonker's assistance in the tedious classification and gridding of the data was invaluable and very much appreciated.

REFERENCES

Anthes, R. A., and Johnson, D. R., "Generation of Available Potential Energy in Hurricane Hilda (1964)," *Monthly Weather Review*, Vol. 96, No. 5, May **1968**, pp. 291–302.

Davis, P. A., "An Analysis of the Atmospheric Heat Budget," *Journal of the Atmospheric Sciences*, Vol. 20, No. 1, Jan. **1963**, pp. 5–22.

Dutton, J. A., and Johnson, D. R., "The Theory of Available Potential Energy and a Variational Approach to Atmospheric Energetics," *Advances in Geophysics*, Vol. 12, **1967**, pp. 333–436.

Hanson, K. J., Vonder Haar, T. H., and Suomi, V. E., "Reflection of Sunlight to Space and Absorption by the Earth and Atmosphere Over the United States During Spring 1962," *Monthly Weather Review*, Vol. 95, No. 6, June **1967**, pp. 354–362.

Korb, G., and Möller, F., "Theoretical Investigations on Energy Gain by Absorption of Solar Radiation in Clouds," *Final Technical Report*, Contract No. DA–91–591–EUC–1612, Ludwig-Maximilians-Universität Meteorologisches Institüt, München, Germany, **1962**, 185 pp.

List, R. J., *Smithsonian Meteorological Tables*, Smithsonian Institution, Washington, D.C., **1951**, 527 pp.

London, J., "A Study of the Atmospheric Heat Balance," *Final Report*, Contract No. AF 19(122)—165, Research Division, College of Engineering, New York University, July **1957**.

Mugge, R., and Möller, F., "Zur Berechnung von Strahlungsströmen und Temperaturänderungen in Atmosphären vol beliebigem Aufbau," (On the Computation of Radiation Currents and Temperature Variations in Atmospheres in Buildings of Any Size), *Zeitung der Geophysik*, Vol. 8, **1963**, pp. 53–64.

Panofsky, H., *Introduction to Dynamic Meteorology*, The Pennsylvania State University, University Park, **1956**, 243 pp., (see p. 111).

Petterssen, S., *Weather Analysis and Forecasting*, McGraw-Hill Book Co., Inc., New York, **1956**, 2 vols., 428 pp. and 266 pp.

Petterssen, S., Bradbury, D. L., and Pedersen, K., "The Norwegian Cyclone Models in Relation to Heat and Cold Sources," *Geofysiske Publikasjoner*, Oslo, Vol. 24, **1962**, pp. 243–280.

Suomi, V. E., and Chen, W. C., "Horizontal Variation of Infrared Cooling and the Generation of Eddy Available Potential Energy," *Journal of the Atmospheric Sciences*, Vol. 20, No. 1, Jan. **1963**, pp. 62–65.

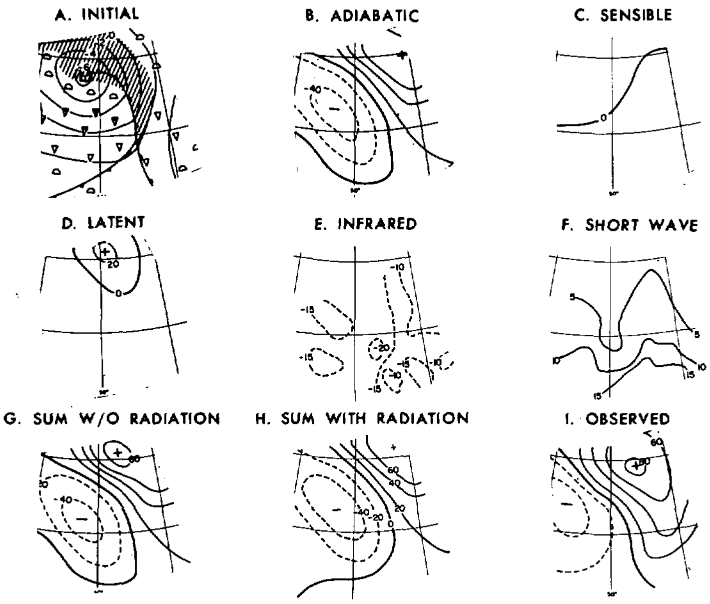

FIGURE 16.—Computation of 3-hr thickness change of 1000–500-mb layer, occluded cyclone case (1200 GMT, Jan. 28, 1958). (A) 1000-mb surface (hundreds of feet); (B) thickness change (ft/3 hr) due to adiabatic motion; (C) thickness change due to sensible heat flux from the surface; (D) thickness change due to release of latent heat; (E) thickness change due to infrared cooling; (F) thickness change due to short-wave warming; (G) sum of B, C, and D; (H) sum of B, C, D, E, and F; (I) observed thickness change. (Analyses A, B, C, D, G, and I taken from Petterssen et al., 1962.)

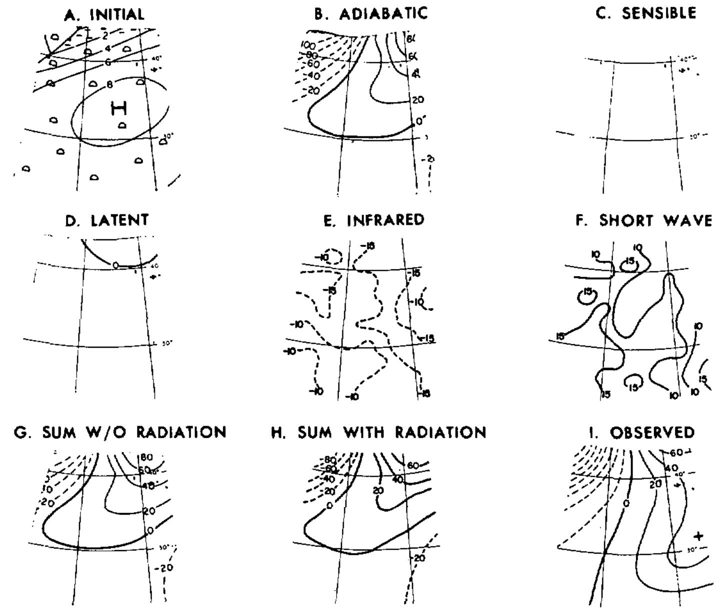

FIGURE 17.—Computation of 3-hr thickness change of 1000–500-mb layer, anticyclone case (1200 GMT, Jan. 5, 1958). (A) 1000-mb surface (hundreds of feet); (B) thickness change (ft/3 hr) due to adiabatic motion; (C) thickness change due to sensible heat flux from the surface; (D) thickness change due to release of latent heat; (E) thickness change due to infrared cooling; (F) thickness change due to short-wave warming; (G) sum of B, C, and D; (H) sum of B, C, D, E, and F; (I) observed thickness change. (Analyses A, B, C, D, G, and I taken from Petterssen et al., 1962.)

TABLE 3.—*Extreme values of contours for thickness tendency comparisons*

	Nascent (ft/3 hr)	Warm sector (ft/3 hr)	Occluded (ft/3 hr)	Anti-cyclone* (ft/3 hr)
B. Adiabatic	−120	−180	+60	−60
C. Sensible	+60	+20	0	0
D. Latent	+20	+20	+20	0
E. Infrared	−20	−20	−20	−15
F. Short-wave	+20	+20	+15	+55
G. Sum w/o radiation	+60	−180	+80	+60
H. Sum with radiation	+60	−180	+60	+80
I. Sum observed	+80	−200	+80	+60

*The anticyclone maxima were chosen for the area under direct influence of the high-pressure system and not for the cold front visible in the northwest corner of figure 17A.

TABLE 4.—*Radiative-induced vorticity change at the surface* (sec^{-2})

$-\frac{R}{f c_p}\nabla^2(\log\frac{p}{p_0}(\text{radiative cooling field}))$			
	Short-wave	Infrared	Short-wave+ infrared
Nascent cyclone	4.6×10^{-10}	1.4×10^{-10}	6.0×10^{-10}
Warm sector cyclone	1.1×10^{-10}	0.1×10^{-10}	1.2×10^{-10}
Occluded cyclone	-1.7×10^{-10}	0.1×10^{-10}	-1.6×10^{-10}
Anticyclone	-0.1×10^{-10}	0.7×10^{-10}	0.6×10^{-10}

Sutcliffe, R. C., "A Contribution to the Problem Development," *Quarterly Journal of the Royal Meteorological Society*, Vol. 73, No. 317/318, July/Oct. **1947**, pp. 370–383.
Tanner, C. B., Businger, J. A., and Kuhn, P. M., "The Economical Net Radiometer," *Journal of Geophysical Research*, Vol. 65, No. 11, Nov. **1960**, pp. 3657–3667.
Vonder Haar, T. H., Space Science and Engineering Center, University of Wisconsin, Madison, **1968**, (personal communication).
Yamamoto, G., "Direct Absorption of Solar Radiation by Atmospheric Water Vapor, Carbon Dioxide and Molecular Oxygen," *Journal of the Atmospheric Sciences*, Vol. 19, No. 2, Mar. **1962**, pp. 182–188.

[*Received September 26, 1968; revised June 16, 1969*]